THE JOURNAL OF PHYSICAL CHEMISTRY LETTERS
A JOURNAL OF THE AMERICAN CHEMICAL SOCIETY

pubs.acs.org/JPCL Letter

Enhancing Circularly Polarized Luminescence Dissymmetry Factor of Chiral Cylindrical Molecules to −0.56 through Intramolecular Short-Range Charge Transfer

Tengfei He, Wenkai Zhao, Menglu Lin, Bing Sun, Yongsheng Chen, Hao-Li Zhang,* and Guankui Long*

Cite This: J. Phys. Chem. Lett. 2024, 15, 9844−9851 Read Online

ACCESS | Metrics & More | Article Recommendations | Supporting Information

ABSTRACT: High-performance circularly polarized luminescent (CPL) materials have received wide attention recently by virtue of broad application in circularly polarized light-emitting diodes, 3D display, and encryption. Reaching both high luminescence efficiency and strong luminescence dissymmetry factor (g_{lum}) is still a challenging goal that requires continuous efforts. Herein, we performed a systematic theoretical investigation on the chiroptical properties of helical cylindrical molecules (−)-[4]cyclo-2,6-anthracene [(−)-[4]$CA_{2,6}$] and (*P*)-[4]cyclo-2,8-chrysenylene [(*P*)-[4]$CC_{2,8}$], and found that the unique and symmetric cylindrical structure could make the transition dipole moment components offset along the cylindrical surface but concentrated along the vertical central axis. This structural superiority contributes the collinear electric and magnetic transition dipole moment vectors and thus the large g_{lum}. Based on the results of decomposed transition dipole moment vectors to individual atoms, an effective strategy to enhance the g_{lum} through introducing intramolecular short-range charge transfer by embedding B,N atoms is proposed. The decreased electric transition dipole moment and well-kept magnetic transition dipole moment enable the g_{lum} of B,N-embedded designed molecules (−)-[4]$CA_{2,6}$-4BN and (*P*)-[4]$CC_{2,8}$-4BN up to −0.31 and −0.56, respectively. This molecular-insight investigation deepens the understanding of the structure−property relationship and provides efficient guidance for improving g_{lum} of CPL materials.

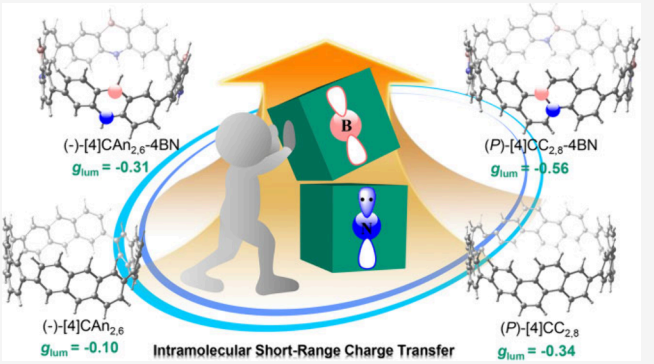

Circularly polarized luminescent (CPL) materials, with the ability of directly emitting left- or right-handed circularly polarized light,[1,2] have a broad foreground in 3D displays, data storage, biological probes, and asymmetric photosynthesis.[3−7] Benefiting from the superiorities of high-performance and simple device architectures, circularly polarized organic light-emitting diodes (CP-OLEDs) have attracted enormous research interests.[8,9] To achieve the high-performance of fast exciton conversion and a high degree of circular polarization, it is critical to simultaneously obtain both high photoluminescence quantum efficiency (Φ_F) and strong luminescence dissymmetry factor (g_{lum}). In quantum chemistry, Φ_F is determined by the radiative and nonradiative transition rates (k_r and k_{nr}) as in eq 1,

$$\Phi_F = \frac{k_r}{k_r + k_{nr}} \tag{1}$$

Apparently, a high Φ_F needs a large k_r and small k_{nr}; the strong correlation of Φ_F and g_{lum} can be achieved with the electric transition dipole moment ($\boldsymbol{\mu}_e$) due to the simplified relationship of $k_r \propto \tilde{\nu}^3 \times |\boldsymbol{\mu}_e|^2$ ($\tilde{\nu}$: emission energy, details in Computational Methods),[10,11] and g_{lum} is quantified as eq 2,[12,13]

$$g_{lum} = \frac{4|\boldsymbol{\mu}_e||\boldsymbol{\mu}_m|\cos\theta}{|\boldsymbol{\mu}_e|^2 + |\boldsymbol{\mu}_m|^2} \tag{2}$$

where $\boldsymbol{\mu}_m$ is the magnetic transition dipole moment vector and θ is the angle between $\boldsymbol{\mu}_e$ and $\boldsymbol{\mu}_m$ vectors. In the traditional achiral molecule system, $\boldsymbol{\mu}_m$ is always perpendicular to the plane determined by the displacement vector ($\boldsymbol{r}$) and $\boldsymbol{\mu}_e$ due to the right-hand rule (Figure 1a). In this instance, cos θ is always zero ($\boldsymbol{\mu}_e \perp \boldsymbol{\mu}_m$), leading to the invalid CPL. While in the chiral system, the helical trajectory of electron motion enables the induced $\boldsymbol{\mu}_m$ to possess nonzero collinear projections relative to the $\boldsymbol{\mu}_e$ (Figure 1a). This is the main origin of the circularly

Received: July 10, 2024
Revised: September 10, 2024
Accepted: September 17, 2024
Published: September 19, 2024

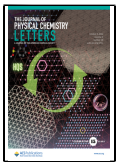

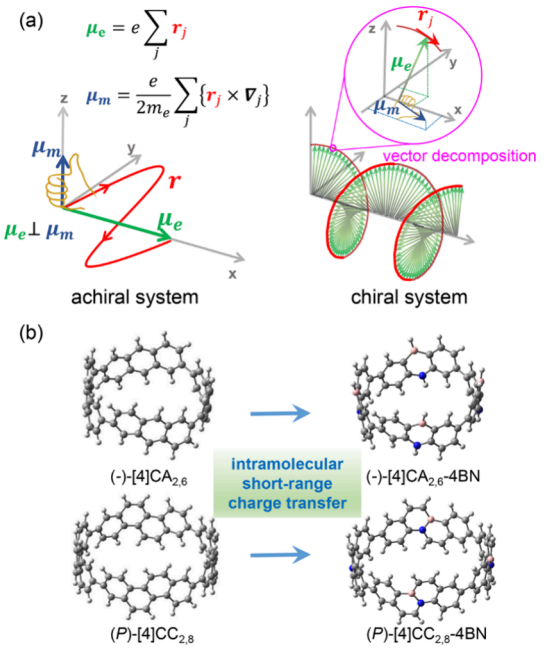

Figure 1. (a) Illumination of the electric transition dipole moment ($\boldsymbol{\mu}_e$) and magnetic transition dipole moment ($\boldsymbol{\mu}_m$) in achiral and chiral systems. (b) The optimized S_1 geometries of (−)-[4]$CA_{2,6}$, (*P*)-[4]$CC_{2,8}$, (−)-[4]$CA_{2,6}$-4BN, and (*P*)-[4]$CC_{2,8}$-4BN.

polarized luminescence presented by chiral molecules. However, most light emitting materials are magnetic dipole forbidden with small $|\boldsymbol{\mu}_m|$,[11] making $|g_{lum}|$ generally within the range of 10^{-4}−10^{-2}.[4,8,9] Thus, effective molecular design strategies for achieving both large g_{lum} and high Φ_F are urgently needed.

Among the investigated chiral organic molecules, helical chiral single-wall carbon nanotube (SWCNT) molecules of (−)-[4]cyclo-2,6-anthracene [(−)-[4]$CA_{2,6}$] and (*P*)-[4]cyclo-2,8-chrysenylene [(*P*)-[4]$CC_{2,8}$] were reported, which showed particularly high g_{lum} of −0.103 and −0.152.[14,15] The excellent chiroptical properties of these two molecules called our attention to further explore the structure−property relationship and effective improvement strategy. Herein, we performed a detailed theoretical study and unveiled the origin of the strong g_{lum} values of these cylindrical molecules. According to the profound investigation of the transition dipole moment, the unique and symmetric cylindrical structure contributes not only the colinear vectors of electric and magnetic transition dipole moments but also the amplification of magnetic transition dipole moments, leading to excellent $|g_{lum}|$. Additionally, an intramolecular short-range charge transfer (SRCT)[16] strategy by embedding B,N atoms into these cylindrical structures was performed, leading to a reduced electric transition dipole moment and promoting g_{lum} of the designed (−)-[4]$CA_{2,6}$-4BN and (*P*)-[4]$CC_{2,8}$-4BN up to −0.31 and −0.56, respectively. This research offers a new guideline for developing high g_{lum} organic CPL materials.

The special cylindrical structures of these molecules show a close correlation with the circularly polarized luminescence properties. As shown in Figure 1b, the optimized S_1 geometries of both (−)-[4]$CA_{2,6}$ and (*P*)-[4]$CC_{2,8}$ are regular cylindrical structures with diameters of 11.03 and 13.56 Å, respectively. There are four equivalent segments enclosing the cylinder possessing homogenic dihedral angles of 44.25° for (−)-[4]$CA_{2,6}$ and 35.78° for (*P*)-[4]$CC_{2,8}$ (Figure S1), which enables the electrons symmetrically and uniformly spreading along the sp^2-carbon molecular skeleton (as the electrostatic potential maps shown in Figures 2 and S2). Both

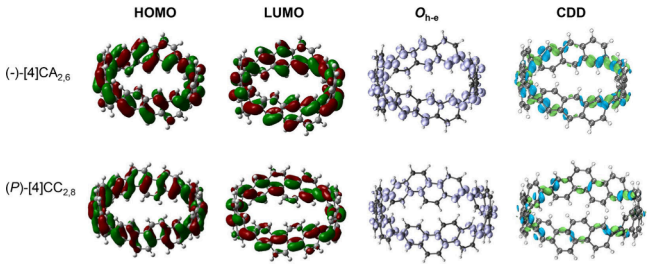

Figure 2. HOMO and LUMO distributions (isovalue = 0.02), the overlap ($O_{h\text{-}e}$), and charge density difference (CDD) of hole and electron for (−)-[4]$CA_{2,6}$ and (*P*)-[4]$CC_{2,8}$ in the $S_1 \rightarrow S_0$ transition (isovalue = 0.001, green/blue parts indicating the increased/decreased electron density).

the highest occupied molecular orbital (HOMO) and the lowest unoccupied molecular orbital (LUMO) are located at the π orbital of the curved part, which would result in the distinct spiral contributions during the electronic transition (vide infra). Hence, the modifications on the individual segment or tuning the curvature of the cylinder should be an effective strategy to improve the performance of the circularly polarized luminescence.

The detailed $S_1 \rightarrow S_0$ transition information is summarized in Table S1. The calculated fluorescence wavelengths are 565.82 nm for (−)-[4]$CA_{2,6}$ and 443.56 nm for (*P*)-[4]$CC_{2,8}$, which are in good agreement with their corresponding experimental results of 536 and 443 nm, respectively.[14,15] Combined with the natural transition orbital (NTO) analysis (Figure S3), it is obvious that the fluorescence emissions in both (−)-[4]$CA_{2,6}$ and (*P*)-[4]$CC_{2,8}$ are characterized as localized excitation, even though there are several transition contributions for (*P*)-[4]$CC_{2,8}$. The complicated components make the overlap of hole and electron ($O_{h\text{-}e}$) in (*P*)-[4]$CC_{2,8}$ (0.8024 au) much smaller than that of (−)-[4]$CA_{2,6}$ (0.8509 au) (Figure 2), which is also responsible for the smaller electric transition dipole moment and oscillator strength (*f*) in (*P*)-[4]$CC_{2,8}$ (Table S2). This is due to $O_{h\text{-}e}$ significantly influencing the magnitude of $|\boldsymbol{\mu}_e|$ based on the following relationships:[10,17,18]

$$|\boldsymbol{\mu}_e| = \iint \phi_h(\boldsymbol{r}_1)\phi_e(\boldsymbol{r}_2)|\boldsymbol{r}_2 - \boldsymbol{r}_1|\phi_h(\boldsymbol{r}_2)\phi_e(\boldsymbol{r}_1)\,d\boldsymbol{r}_1\,d\boldsymbol{r}_2$$

$$|\boldsymbol{\mu}_e| = \sqrt{\frac{3he^2}{8\pi^2 m_e c\tilde{\nu}}}\cdot f$$

Then, the charge density differences (CDDs) between the hole and electron of the $S_1 \rightarrow S_0$ transition are obtained and shown in Figure 2, clearly showing that gaining and losing electrons take place along the inner wall of the cylindrical skeleton. This is also direct evidence that the curvature seriously influences the transition dipole moment and further the luminescence dissymmetry factor.[19,20]

According to eq 2, the chiroptical properties are closely associated with $\boldsymbol{\mu}_e$ and $\boldsymbol{\mu}_m$. Here, we decompose the transition dipole moment density into the contributions from *X*, *Y*, and *Z* coordinate axes (as shown in Figures 3 and S4). In quantum

https://doi.org/10.1021/acs.jpclett.4c02023
J. Phys. Chem. Lett. 2024, 15, 9844−9851

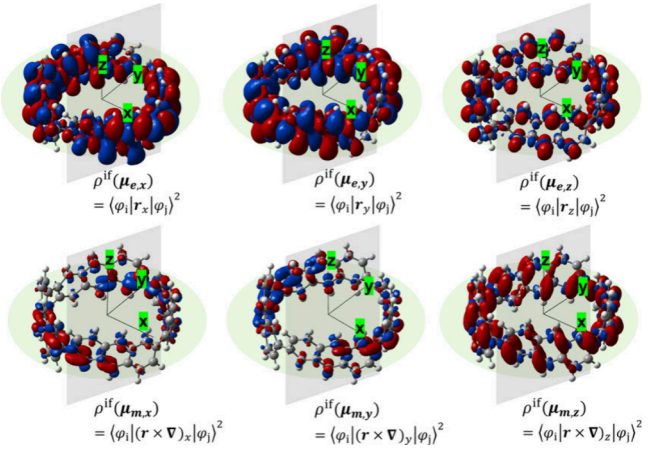

Figure 3. Breakdown analysis of electric transition dipole moment density (isovalue = 0.001) and magnetic transition dipole moment density (isovalue = 0.007) of (−)-[4]$CA_{2,6}$. Positive parts are shown in blue, and negative parts are shown in red.

chemistry, the electric transition dipole moment vector $\boldsymbol{\mu}_e$ is the product of displace operator and wave function of the initial ($|\varphi_i\rangle$) and final (($|\varphi_f\rangle$) states ($\boldsymbol{\mu}_e = \langle\varphi_i|er|\varphi_f\rangle$), and the magnetic transition dipole moment vector $\boldsymbol{\mu}_m$ is the corresponding result from angular momentum operator $\boldsymbol{L}$ $\left(\boldsymbol{\mu}_m = \langle\varphi_i|\boldsymbol{L}|\varphi_f\rangle = \left\langle\varphi_i\left|\frac{e}{2mc}\boldsymbol{r}\times\nabla\right|\varphi_f\right\rangle\right)$.[11] As shown in Figure 3, the central axis of the cylindrical molecule is along the Z-axis, and the four homogenic segments are symmetric in the X/Y direction. Thus, the transition dipole moment density along the X/Y axis positive and negative directions have the same components, so the final results of $\boldsymbol{\mu}_e$ and $\boldsymbol{\mu}_m$ along the X/Y direction cancel out each other to zero (Table S2), while the transition dipole moment contributions on the Z-axis accumulate continuously, leading to the large values of the collinear $\boldsymbol{\mu}_e$ and $\boldsymbol{\mu}_m$. The superiority of the unique and symmetric cylindrical structure is conducive to tuning $\boldsymbol{\mu}_e$ and $\boldsymbol{\mu}_m$ to enhance the luminescence dissymmetry factor. The calculated g_{lum} values are −0.10 for (−)-[4]$CA_{2,6}$ and −0.34 for (P)-[4]$CC_{2,8}$, which is very excellent among the chiral organic fluorescent materials. The structural origins of the strong g_{lum} and improvement strategy are further investigated thereinafter.

According to eq 2, a pair of perfectly matched $\boldsymbol{\mu}_e$ and $\boldsymbol{\mu}_m$ is decisive for g_{lum}. Based on the homogenic cylindrical structure, we decompose the transition dipole moment vector into the contributions of four segments, and further, the atom contributions in a single segment are also obtained to deeply investigate the relationship between molecular structure and chiroptical properties. Here, we take the (−)-[4]$CA_{2,6}$ as an example (Figure 4); it is obvious that the total transition dipole moment is along the central axis of the cylindrical framework, while the separate transition dipole moment segment vector contributions attach the plane and possess the angles of 28.36°/5.73°, deviating from the total $\boldsymbol{\mu}_e/\boldsymbol{\mu}_m$ vectors. The across segment vector contributions orient the opposite directions and cancel out each other at the X or Y axis, which is in accordance with the result of transition dipole moment density analysis. Then, the contributions from atoms of an anthracene segment are also obtained. The atom contribution for $\boldsymbol{\mu}_e$ is nearly perpendicular to the curved plane while that of $\boldsymbol{\mu}_m$ is closely in parallel (as shown in Figure 4). The almost vertical oriented $\boldsymbol{\mu}_e$ and $\boldsymbol{\mu}_m$ vectors of each atom's contribution give intuitive expression of the right-hand rule. Then, a vector projection exploration is carried out for the atom transition dipole moment vector onto the total transition dipole moment vector. It is evident that almost all $\boldsymbol{\mu}_m$ vectors form carbon atoms accumulating together, resulting in the large $|\boldsymbol{\mu}_m|$, while some opposite $\boldsymbol{\mu}_e$ vectors form atoms lower down the total $|\boldsymbol{\mu}_e|$. In contrast with a similar transition dipole moment investigation of (P)-[4]$CC_{2,8}$ (Figure S5), a reduced $\boldsymbol{\mu}_e$ is found due to the more symmetrically positive and negative contributions of carbon atoms and then offsetting in the segment. Compared to the transition dipole moments of (−)-[4]$CA_{2,6}$, the decreased $|\boldsymbol{\mu}_e|$ together with a slightly increased $|\boldsymbol{\mu}_m|$ is responsible for the three times larger g_{lum} for (P)-[4]$CC_{2,8}$ (Table S2).

Improving the $|g_{lum}|$ up to the highest limit value of 2 is a continuous challenge for chiral organic fluorescent molecules.[4] The above-mentioned transition dipole moment investigation arouses some effective structural design principles for these kinds of cylindrical molecules. As shown in eq 2, g_{lum} is determined by the $\boldsymbol{\mu}_e$ and $\boldsymbol{\mu}_m$ vectors, and the value of $|\boldsymbol{\mu}_e|$ is generally evidently larger than $|\boldsymbol{\mu}_m|$ (details in Computational Methods). The effective design strategy is decreasing $|\boldsymbol{\mu}_e|$ while increasing $|\boldsymbol{\mu}_m|$, namely, increasing $|\boldsymbol{\mu}_m|/|\boldsymbol{\mu}_e|$ under the simplified relationship of $|g_{lum}| \propto |\boldsymbol{\mu}_m|/|\boldsymbol{\mu}_e|$. To our knowledge, the charge transfer transition generally holds a smaller electric transition dipole moment than that of localized excitation transition due to reducing the overlap of hole and electron wave functions.[17,21] As for the (−)-[4]$CA_{2,6}$, the contributions from the numbered 2, 4, 6, 9, 11, and 13 C atoms for $\boldsymbol{\mu}_e$ can be further reduced (the vector projection from atoms depicted in Figure 4). It is noteworthy that these atoms are also the main contributions of $O_{h\text{-}e}$ as shown in Figure 2. Inspired by efficient reduction of $O_{h\text{-}e}$ via intramolecular short-range charge transfer (SRCT), the molecular engineering regulated by using the lone pair electrons of N atom and empty orbit of B atom might be a valid way to decrease the electric transition dipole moment.[22−26]

Herein, we introduce the SRCT through symmetrically embedding the B and N atoms in the individual segment on the basis of (−)-[4]$CA_{2,6}$ and (P)-[4]$CC_{2,8}$, and the designed structures are shown in Figure S6. For the designed molecules, their frontier molecular orbital and electrostatic potential maps (Figures S2 and S6) reveal that the uniformed electron distribution is clearly tuned as HOMO focusing on the electron-rich N atoms, while LUMO focusing on the electron-deficient B atoms. The overlap integrals are 0.7646/0.7200 au for (−)-[4]$CA_{2,6}$-4BN/(P)-[4]$CC_{2,8}$-4BN; thus, the electric transition dipole moment could be effectively decreased (Tables S2 and S3). The short-range charge transfer transition will also be introduced in the fluorescence emission, and the natural transition orbital and charge density difference analyses (Figures S4−S7) further validate the process of charge transfer occurring onto the curved segment, especially the B,N part. These detailed analyses of electric and magnetic transition dipole moment unveil the following.

(i) The designed B,N-embedded molecules present a stable cylindrical structure, maintaining the transition dipole moment distributions offset to zero at the X/Y direction and accumulate along the Z-axis. Namely, the superiority of collinear $\boldsymbol{\mu}_e$ and $\boldsymbol{\mu}_m$ perfectly remains, and an obvious positive correlation of $|g_{lum}|$ and $|\boldsymbol{\mu}_m|/|\boldsymbol{\mu}_e|$ is found among these cylindrical molecules (Table S4).

https://doi.org/10.1021/acs.jpclett.4c02023
J. Phys. Chem. Lett. 2024, 15, 9844−9851

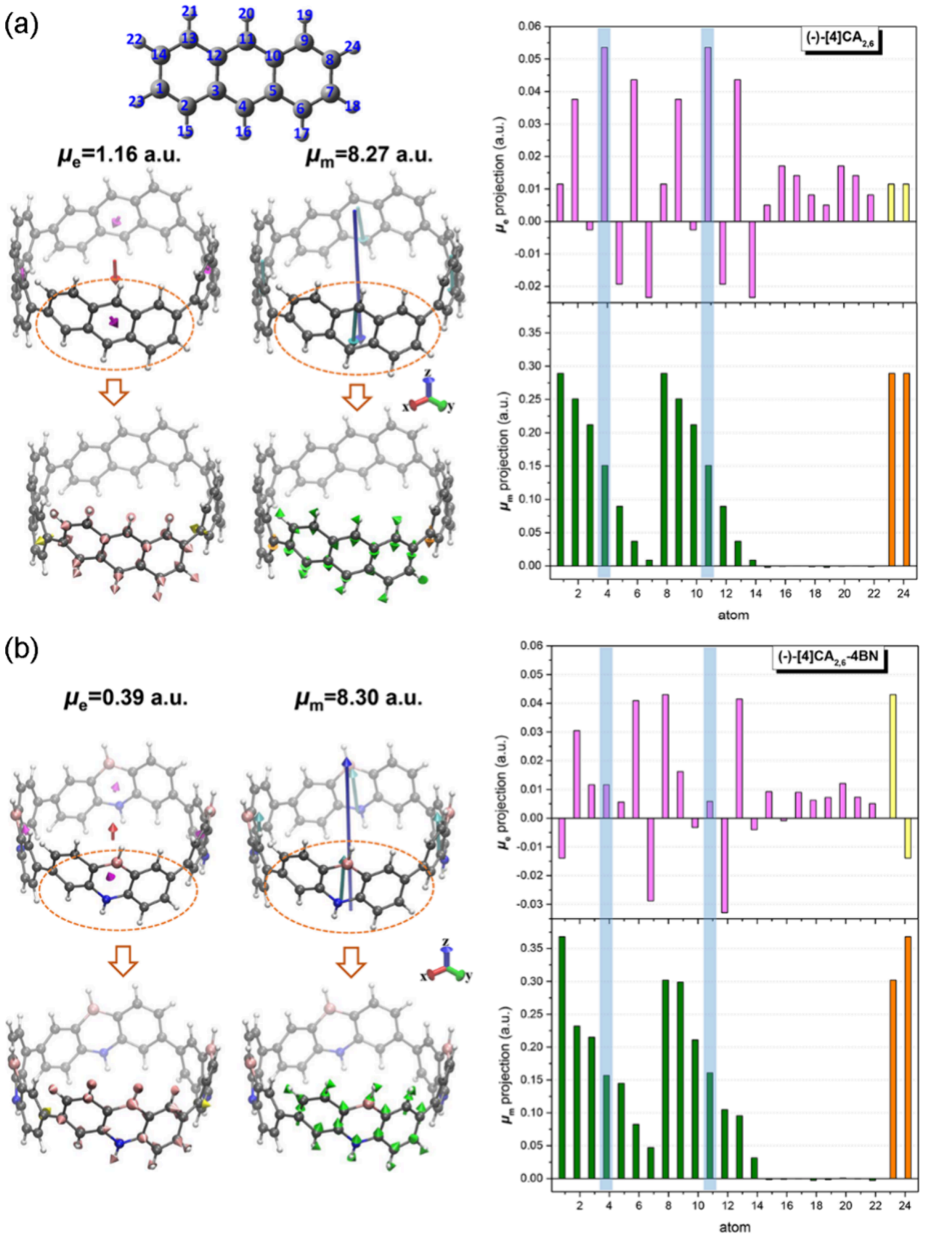

Figure 4. Decomposition of the transition dipole moment vector as segments and atoms contributions for (−)-[4]CA$_{2,6}$ (a) and (−)-[4]CA$_{2,6}$-4BN (b), together with the vector projection from the atom contribution onto the total transition dipole moment vector (in the units of au). Note: the arrows for the atom transition dipole moment vector are magnified three times for clarity.

https://doi.org/10.1021/acs.jpclett.4c02023
J. Phys. Chem. Lett. 2024, 15, 9844−9851

(ii) The SRCT induced by the electron-rich N atoms and electron-deficient B atoms effectively reduces the overlap between hole and electron, resulting in the decreased $\boldsymbol{\mu}_e$. Meanwhile, $\boldsymbol{\mu}_m$ keeps or even increases in the electronic excitation process.

(iii) The values of g_{lum} are −0.31 for (−)-[4]$CA_{2,6}$-4BN and −0.56 for (*P*)-[4]$CC_{2,8}$-4BN, which are significantly increased relative to those of (−)-[4]$CA_{2,6}$ and (*P*)-[4]$CC_{2,8}$.

Besides the luminescence dissymmetry factor (g_{lum}), there is another critical factor affecting the performance of CP-OLEDs, namely, the fluorescence efficiency (Φ_F). Φ_F is generally determined by the radiative transition rate k_r and the nonradiative transition rate k_{nr} as shown in eq 1. Based on the discussion above, we know that the magnetic transition dipole moment is non-negligible, especially for chiral OLED molecules. Here, we calculated the k_r under the consideration of magnetic transition dipole moment, as shown in eq 3:[27,28]

$$k_r = \frac{16\pi^3}{3h\varepsilon_0}\tilde{\nu}^3(|\boldsymbol{\mu}_e|^2 + |\boldsymbol{\mu}_m|^2 \mp 2R) \tag{3}$$

where the rotatory strength (R) can be calculated by the imaginary part of the scalar product between the $\boldsymbol{\mu}_e$ and $\boldsymbol{\mu}_m$ vectors:[4]

$$R = Im(\boldsymbol{\mu}_e \cdot \boldsymbol{\mu}_m) = |\boldsymbol{\mu}_e||\boldsymbol{\mu}_m|\cos\theta \tag{4}$$

The related important parameters of k_r are calculated and summarized in Table S3; the k_r generally depends on the emission energy and electric transition dipole moment according to the Einstein spontaneous emission theory. On the condition of greatly larger $|\boldsymbol{\mu}_e|^2$ of (−)-[4]$CA_{2,6}$ [(−)-[4]-$CA_{2,6}$: 86 827.15 × 10^{-40} esu^2·cm^2; (*P*)-[4]$CC_{2,8}$: 21 107.65 × 10^{-40} esu^2·cm^2], an order of magnitude higher k_r [1.42 × 10^7/1.58 × 10^7 s^{-1} for (−)-[4]$CA_{2,6}$ and 6.35 × 10^6/8.92 × 10^6 s^{-1} for (*P*)-[4]$CC_{2,8}$] is determined mainly by $|\boldsymbol{\mu}_e|^2$. However, for the slightly smaller $|\boldsymbol{\mu}_e|^2$ of (*P*)-[4]$CC_{2,8}$-4BN, its stronger $|\boldsymbol{\mu}_m|^2$ could effectively increase, leading to its k_r being larger than that of (−)-[4]$CA_{2,6}$-4BN (Table S3). Thus, it is important to take the magnetic transition dipole moment into consideration for the determination of radiative transition rate. Another key factor for fluorescence efficiency is nonradiative transition rate (k_{nr}), which could be seriously restrained by large emission energy and reduced electron-vibration coupling according to the energy gap law.[29−31] From Table S3, all the investigated cylindrical molecules possess enhanced emission energy [(*P*)-[4]$CC_{2,8}$: 2.80 eV; (−)-[4]$CA_{2,6}$: 2.19 eV; (*P*)-[4]$CC_{2,8}$-4BN: 3.22 eV; (−)-[4]$CA_{2,6}$-4BN: 2.82 eV], which is beneficial for suppressing the nonradiative transition according to the exponential dependence of $k_{nr} \sim \exp(-\beta\cdot\tilde{\nu})$ (β is the related to electron-vibration coupling parameter). Here, we concentrate on the electron-vibration coupling via the reorganization energy ($\lambda_{S_1 \to S_0}$) between S_1 and S_0 states for the k_{nr} investigation. The total $\lambda_{S_1 \to S_0}$ is 0.1809 eV for (−)-[4]$CA_{2,6}$, 0.1780 eV for (*P*)-[4]$CC_{2,8}$, 0.1053 eV for (−)-[4]$CA_{2,6}$-4BN, and 0.1387 eV for (*P*)-[4]$CC_{2,8}$-4BN (Figure S8). Both the high emission energy and decreased reorganization energy indicate that the k_{nr} of the designed (−)-[4]$CA_{2,6}$-4BN and (*P*)-[4]$CC_{2,8}$-4BN would be smaller than that of (−)-[4]$CA_{2,6}$ and (*P*)-[4]$CC_{2,8}$. Obviously, the design strategy of SRCT through symmetrically embedding the B and N atoms in the individual segment shows advantages in improving the fluorescence efficiency for these types of cylindrical molecules.

Additionally, the absorption dissymmetry factors (g_{abs}) were calculated with similar methods. The values of g_{abs} are −0.09 for (−)-[4]$CA_{2,6}$, −0.33 for (*P*)-[4]$CC_{2,8}$, −0.14 for (−)-[4]-$CA_{2,6}$-4BN, and −0.45 for (*P*)-[4]$CC_{2,8}$-4BN. The designed molecules through the B,N-embedded strategy also show higher g_{abs}. Then, the relation between absorption and luminescence dissymmetry factor is then further explored in detail. As summarized in Table S4, a larger $|g_{abs}|$ always presents a larger $|g_{lum}|$ for these studied cylindrical molecules, which could be attributed to their reduced nonradiative transition and high fluorescence efficiency. Further, it is found that the difference of dissymmetry factor Δg ($\Delta g = |g_{lum} - g_{abs}|$) has an opposite trend relative to that of ($\lambda_{S_1 \to S_0}$). This should be rationalized to the well suppressed nonradiative transition, especially structural deformation between excited and ground states.

In summary, the origin of the strong luminescence dissymmetry factor of the chiral cylindrical molecules has been systematically investigated through DFT and TD-DFT calculations. The unique and symmetric cylindrical structures of (−)-[4]$CA_{2,6}$ and (*P*)-[4]$CC_{2,8}$ have a perfect configuration, which leads to the transition dipole moment densities with the same sizes but opposite signs along the *X*/*Y* axis while accumulating along the *Z* axis. Thus, the electric transition dipole moment and magnetic transition dipole moment vectors of *X* and *Y* directions cancel out each other to zero; at the same time, they concentrate on the *Z* axis, resulting in the collinear transition dipole moment vectors and finally large g_{lum}. We decompose the transition dipole moment vectors into the individual atom contribution and find the C atoms at the curved framework with more contributions to the electric transition dipole moment, so that an effective way of slightly reducing the electric transition dipole moment by embedding B,N atoms is performed to further improve g_{lum}. Then, both the charge density difference and the electrostatic potential results of the designed (−)-[4]$CA_{2,6}$-4BN and (*P*)-[4]$CC_{2,8}$-4BN indicate that short-range charge transfer is successful in decreasing the overlap of the hole and electron and further reducing the electric transition dipole moment. Together with the well maintained magnetic transition dipole moment, the g_{lum} of the B,N-embedded designed molecule is promoted to −0.31 for (−)-[4]$CA_{2,6}$-4BN and −0.56 for (*P*)-[4]$CC_{2,8}$-4BN. For these excellent chiroptical cylindrical molecules, the strong magnetic transition dipole moment could make a non-negligible contribution to the determination of radiative transition rate. g_{abs} and g_{lum} have similar trends, and the difference of dissymmetry factor Δg ($\Delta g = |g_{lum} - g_{abs}|$) shows an opposite correlation relative to reorganization energy. This detailed theoretical investigation expands the exploration of the structure−property relationship for circularly polarized luminescent helical cylindrical molecules and provides a new design strategy for improving their luminescence dissymmetry factor.

COMPUTATIONAL METHODS

In this work, the density functional theory (DFT)[32] and time-dependent DFT (TD-DFT) calculations are performed to obtain the equilibrium geometries and the vibration frequencies of the ground state (S_0) and the lowest singlet excited state (S_1) of the investigated molecules at the B3LYP/6-31G(d)[33] method within the Gaussian 16 package.[34] To

https://doi.org/10.1021/acs.jpclett.4c02023
J. Phys. Chem. Lett. 2024, 15, 9844−9851

accurately predict the fluorescence and CPL properties, various functionals and basis sets are benchmarked on (*P*)-[4]$CC_{2,8}$. As shown in Table S5, the calculated wavelength of 443.56 nm within the TD-BMK/6-311G(d,p)[35] under toluene solution (performed by the polarized continuum model (PCM)[36]) coincided very well with the measured 443 nm in the experiment; the calculated g_{lum} of −0.34 was slightly larger than the experimental value of −0.152. We think it is enough to provide believable results, and the following chiroptical properties are investigated on the basis of this method. The further electronic transition properties (such as the overlap and charge density difference of hole and electron, the transition dipole moment density, and the decomposition of the transition dipole moment vector) are investigated by the Multiwfn package.[37]

According to the time-dependent perturbation theory, fluorescence is treated as an electronic transition from the initial S_1 state ($|\varphi_i\rangle$) to the final ground state ($|\varphi_f\rangle$). The transition probability coefficient ($A_{i\to f}$) can be obtained according to the Einstein spontaneous emission theory based on eq 5:[11]

$$A_{i\to f} = \frac{8\pi^3}{3h^2}\left(|\langle\varphi_i|e\boldsymbol{r}|\varphi_f\rangle|^2 + \left|\left\langle\varphi_i\left|\frac{e}{2mc}\boldsymbol{r}\times\nabla\right|\varphi_f\right\rangle\right|^2 + \frac{3}{10}\pi^3\tilde{\nu}^3|\langle\varphi_i|e\boldsymbol{rr}|\varphi_f\rangle|^2\right) \tag{5}$$

where e is the elementary charge, h is the Planck Constant, m is the electron mass, c is the light velocity, $\tilde{\nu}$ is the emission energy, and $\boldsymbol{r}$ is the placement vector of electron motion. The first item corresponds to the electric transition dipole moment; the second item corresponds to the magnetic transition dipole moment, and the last one is the electric quadrupole transition moment. Their relative order of magnitude in the electromagnetic unit is estimated shown below (exemplified by the results of the H atom).[11]

$$|\langle\varphi_i|e\boldsymbol{r}|\varphi_f\rangle|^2 \sim 6.5\times10^{-36}\ \text{c.g.s.}$$

$$\left|\left\langle\varphi_i\left|\frac{e}{2mc}\boldsymbol{r}\times\nabla\right|\varphi_f\right\rangle\right|^2 \sim 8.7\times10^{-41}\ \text{c.g.s.}$$

$$\frac{3}{10}\pi^3\tilde{\nu}_{i\to f}{}^3|\langle\varphi_i|e\boldsymbol{rr}|\varphi_f\rangle|^2 \sim 6.8\times10^{-43}\ \text{c.g.s.}$$

In the conventional luminescent molecules, due to the small magnetic transition dipole moment or the perpendicularly oriented electric and magnetic transition dipole moment vectors, the effects of the magnetic transition dipole moment on both the chiroptical properties and radiative transition rates are usually negligible, while in the chiral molecules, the relatively strong magnetic transition dipole moment plays a significant role in the photoluminescence and chiroptical properties.

The nonradiative transition rate k_{nr} is always predicted an exponential dependence on the energy gap ($\tilde{\nu}$) and electron-vibration coupling parameter (β) between the S_1 and S_0 states, which could be described as $k_{nr}\sim\exp(-\beta\cdot\tilde{\nu})$ within the energy gap law.[31] Here, the electron-vibration coupling parameter is taken into consideration through the reorganization energy (λ) between the excited state and ground state:

$$\lambda = \sum_j \frac{1}{2}\omega_j{}^2\Delta Q_j{}^2 \tag{6}$$

in which ω_j and ΔQ_j are the frequency and the shift vector of the jth normal mode. λ is obtained via the MOMAP program.[38]

■ ASSOCIATED CONTENT

Supporting Information

The Supporting Information is available free of charge at https://pubs.acs.org/doi/10.1021/acs.jpclett.4c02023.

Fluorescence transition information, electric and magnetic transition dipole moment investigation, natural transition orbital analysis, computation methods benchmark, and coordinates of optimized structures (PDF)

■ AUTHOR INFORMATION

Corresponding Authors

Hao-Li Zhang − *State Key Laboratory of Applied Organic Chemistry, Key Laboratory of Special Function Materials and Structure Design, Ministry of Education, College of Chemistry and Chemical Engineering, Lanzhou University, Lanzhou 730000, China;* orcid.org/0000-0002-6322-5202; Email: haoli.zhang@lzu.edu.cn

Guankui Long − *School of Materials Science and Engineering, Smart Sensing Interdisciplinary Science Center, Tianjin Key Lab for Rare Earth Materials and Applications, Renewable Energy Conversion and Storage Center (RECAST), National Institute for Advanced Materials, Nankai University, 300350 Tianjin, China;* orcid.org/0000-0002-1826-3736; Email: longgk09@nankai.edu.cn

Authors

Tengfei He − *The Centre of Nanoscale Science and Technology and State Key Laboratory of Elemento-Organic Chemistry, Frontiers Science Center for New Organic Matter, College of Chemistry, Nankai University, Tianjin 300071, China; School of Materials Science and Engineering, Smart Sensing Interdisciplinary Science Center, Tianjin Key Lab for Rare Earth Materials and Applications, Renewable Energy Conversion and Storage Center (RECAST), National Institute for Advanced Materials, Nankai University, 300350 Tianjin, China*

Wenkai Zhao − *School of Materials Science and Engineering, Smart Sensing Interdisciplinary Science Center, Tianjin Key Lab for Rare Earth Materials and Applications, Renewable Energy Conversion and Storage Center (RECAST), National Institute for Advanced Materials, Nankai University, 300350 Tianjin, China*

Menglu Lin − *School of Materials Science and Engineering, Smart Sensing Interdisciplinary Science Center, Tianjin Key Lab for Rare Earth Materials and Applications, Renewable Energy Conversion and Storage Center (RECAST), National Institute for Advanced Materials, Nankai University, 300350 Tianjin, China*

Bing Sun − *State Key Laboratory of Applied Organic Chemistry, Key Laboratory of Special Function Materials and Structure Design, Ministry of Education, College of Chemistry and Chemical Engineering, Lanzhou University, Lanzhou 730000, China*

Yongsheng Chen − *The Centre of Nanoscale Science and Technology and State Key Laboratory of Elemento-Organic*

https://doi.org/10.1021/acs.jpclett.4c02023
J. Phys. Chem. Lett. 2024, 15, 9844−9851

Chemistry, Frontiers Science Center for New Organic Matter, College of Chemistry, Nankai University, Tianjin 300071, China; orcid.org/0000-0003-1448-8177

Complete contact information is available at: https://pubs.acs.org/10.1021/acs.jpclett.4c02023

Notes

The authors declare no competing financial interest.

■ ACKNOWLEDGMENTS

The authors gratefully acknowledge the financial support from the NSFC (Grant Numbers: 92256202, U22A20399, 52473305, 12261131500, 52103218) of China, the Fundamental Research Funds for the Central Universities, Nankai University (Grant Number: 023-63223021), and the 111 Project (B18030), the Open Fund of the Key Lab of Organic Optoelectronics and Molecular Engineering of Ministry of Education (No. 53223000122). We gratefully acknowledge HZWTECH for providing computation facilities.

■ REFERENCES

(1) Riehl, J. P.; Richardson, F. S. Circularly polarized luminescence spectroscopy. *Chem. Rev.* **1986**, *86*, 1−16.
(2) Longhi, G.; Castiglioni, E.; Koshoubu, J.; Mazzeo, G.; Abbate, S. Circularly Polarized Luminescence: A Review of Experimental and Theoretical Aspects. *Chirality* **2016**, *28*, 696−707.
(3) Pop, F.; Zigon, N.; Avarvari, N. Main-Group-Based Electro- and Photoactive Chiral Materials. *Chem. Rev.* **2019**, *119*, 8435−8478.
(4) Gong, Z. L.; Zhu, X. F.; Zhou, Z. H.; Zhang, S. W.; Yang, D.; Zhao, B.; Zhang, Y. P.; Deng, J. P.; Cheng, Y. X.; Zheng, Y. X.; Zang, S. Q.; Kuang, H.; Duan, P. F.; Yuan, M. J.; Chen, C. F.; Zhao, Y. S.; Zhong, Y. W.; Tang, B. Z.; Liu, M. H. Frontiers in circularly polarized luminescence: molecular design, self-assembly, nanomaterials, and applications. *Sci. China Chem.* **2021**, *64*, 2060−2104.
(5) Frédéric, L.; Desmarchelier, A.; Favereau, L.; Pieters, G. Designs and Applications of Circularly Polarized Thermally Activated Delayed Fluorescence Molecules. *Adv. Funct. Mater.* **2021**, *31*, 2010281.
(6) Long, G.; Sabatini, R.; Saidaminov, M. I.; Lakhwani, G.; Rasmita, A.; Liu, X.; Sargent, E. H.; Gao, W. Chiral-perovskite optoelectronics. *Nat. Rev. Mater.* **2020**, *5*, 423−439.
(7) Long, G.; Jiang, C.; Sabatini, R.; Yang, Z.; Wei, M.; Quan, L. N.; Liang, Q.; Rasmita, A.; Askerka, M.; Walters, G.; Gong, X.; Xing, J.; Wen, X.; Quintero-Bermudez, R.; Yuan, H.; Xing, G.; Wang, X. R.; Song, D.; Voznyy, O.; Zhang, M.; Hoogland, S.; Gao, W.; Xiong, Q.; Sargent, E. H. Spin control in reduced-dimensional chiral perovskites. *Nat. Photonics* **2018**, *12*, 528−533.
(8) Han, J.; Guo, S.; Lu, H.; Liu, S.; Zhao, Q.; Huang, W. Recent Progress on Circularly Polarized Luminescent Materials for Organic Optoelectronic Devices. *Adv. Opt. Mater.* **2018**, *6*, 1800538.
(9) Zhang, D. W.; Li, M.; Chen, C. F. Recent advances in circularly polarized electroluminescence based on organic light-emitting diodes. *Chem. Soc. Rev.* **2020**, *49*, 1331−1343.
(10) Siddique, Z. A.; Yamamoto, Y.; Ohno, T.; Nozaki, K. Structure-dependent photophysical properties of singlet and triplet metal-to-ligand charge transfer states in copper(I) bis(diimine) compounds. *Inorg. Chem.* **2003**, *42*, 6366−6378.
(11) Xu, G. X.; Li, L. M.; Wang, D. M. *Quantum Chemistry*; Science Press: Beijing, 2007.
(12) Zhang, Y.; Yu, S.; Han, B.; Zhou, Y.; Zhang, X.; Gao, X.; Tang, Z. Circularly polarized luminescence in chiral materials. *Matter* **2022**, *5*, 837−875.
(13) Nordén, B.; Rodger, A.; Dafforn, T. *Linear dichroism and circular dichroism: a textbook on polarized-light spectroscopy*; Royal Society of Chemistry, 2019.
(14) Wang, J.; Zhuang, G.; Chen, M.; Lu, D.; Li, Z.; Huang, Q.; Jia, H.; Cui, S.; Shao, X.; Yang, S.; Du, P. Selective Synthesis of Conjugated Chiral Macrocycles: Sidewall Segments of (−)/(+)-(12,4) Carbon Nanotubes with Strong Circularly Polarized Luminescence. *Angew. Chem., Int. Ed.* **2020**, *59*, 1619−1626.
(15) Sato, S.; Yoshii, A.; Takahashi, S.; Furumi, S.; Takeuchi, M.; Isobe, H. Chiral intertwined spirals and magnetic transition dipole moments dictated by cylinder helicity. *Proc. Natl. Acad. Sci. U.S.A.* **2017**, *114*, 13097−13101.
(16) Huang, Z.; Xie, H.; Miao, J.; Wei, Y.; Zou, Y.; Hua, T.; Cao, X.; Yang, C. Charge Transfer Excited State Promoted Multiple Resonance Delayed Fluorescence Emitter for High-Performance Narrowband Electroluminescence. *J. Am. Chem. Soc.* **2023**, *145*, 12550−12560.
(17) Tsuchiya, Y.; Tsuji, K.; Inada, K.; Bencheikh, F.; Geng, Y.; Kwak, H. S.; Mustard, T. J. L.; Halls, M. D.; Nakanotani, H.; Adachi, C. Molecular Design Based on Donor-Weak Donor Scaffold for Blue Thermally-Activated Delayed Fluorescence Designed by Combinatorial DFT Calculations. *Front. Chem.* **2020**, *8*, 403.
(18) He, T. F.; Ren, A. M.; Chen, Y. N.; Hao, X. L.; Shen, L.; Zhang, B. H.; Wu, T. S.; Zhang, H. X.; Zou, L. Y. Molecular-Level Insight of Cu(I) Complexes with the 7,8-Bis(diphenylphosphino)-7,8-dicarba-nido-undecaborate Ligand as a Thermally Activated Delayed Fluorescence Emitter: Luminescent Mechanism and Design Strategy. *Inorg. Chem.* **2020**, *59*, 12039−12053.
(19) Onaka, Y.; Tanaka, S.; Kobayashi, A.; Matsuno, T.; Isobe, H. A large-bore chiral cylindrical molecule prone to radial deformations. *Tetrahedron Lett.* **2022**, *96*, 153774.
(20) He, T.; Lin, M.; Wang, H.; Zhang, Y.; Chen, H.; Sun, C. L.; Sun, Z.; Wang, X. Y.; Zhang, H. L.; Chen, Y.; Long, G. Chiral Cylindrical Molecule with Absorption Dissymmetry Factor towards Theoretical Limit of 2. *Adv. Theory Simul.* **2024**, *7*, 2300573.
(21) Chen, X.-K.; Kim, D.; Brédas, J.-L. Thermally Activated Delayed Fluorescence (TADF) Path toward Efficient Electroluminescence in Purely Organic Materials: Molecular Level Insight. *Acc. Chem. Res.* **2018**, *51*, 2215−2224.
(22) Cai, X.; Pu, Y.; Li, C.; Wang, Z.; Wang, Y. Multi-Resonance Building-Block-Based Electroluminescent Material: Lengthening Emission Maximum and Shortening Delayed Fluorescence Lifetime. *Angew. Chem., Int. Ed.* **2023**, *135*, No. e202304104.
(23) Wang, L.; Miao, J.; Zhang, Y.; Wu, C.; Huang, H.; Wang, X.; Yang, C. Discrete Mononuclear Platinum(II) Complexes Realize High-Performance Red Phosphorescent OLEDs with EQEs of up to 31.8% and Superb Device Stability. *Adv. Mater.* **2023**, *35*, No. e2303066.
(24) Zhao, K.; Yao, Z. F.; Wang, Z. Y.; Zeng, J. C.; Ding, L.; Xiong, M.; Wang, J. Y.; Pei, J. ″Spine Surgery″ of Perylene Diimides with Covalent B-N Bonds toward Electron-Deficient BN-Embedded Polycyclic Aromatic Hydrocarbons. *J. Am. Chem. Soc.* **2022**, *144*, 3091−3098.
(25) Chen, C.; Du, C. Z.; Wang, X. Y. The Rise of 1,4-BN-Heteroarenes: Synthesis, Properties, and Applications. *Adv. Sci.* **2022**, *9*, No. e2200707.
(26) Franceschini, M.; Crosta, M.; Ferreira, R. R.; Poletto, D.; Demitri, N.; Zobel, J. P.; Gonzalez, L.; Bonifazi, D. peri-Acenoacene Ribbons with Zigzag BN-Doped Peripheries. *J. Am. Chem. Soc.* **2022**, *144*, 21470−21484.
(27) Schellman, J. A. Circular dichroism and optical rotation. *Chem. Rev.* **1975**, *75*, 323−331.
(28) Kubo, H.; Hirose, T.; Nakashima, T.; Kawai, T.; Hasegawa, J. Y.; Matsuda, K. Tuning Transition Electric and Magnetic Dipole Moments: [7]Helicenes Showing Intense Circularly Polarized Luminescence. *J. Phys. Chem. Lett.* **2021**, *12*, 686−695.
(29) Wang, S.-F.; Su, B.-K.; Wang, X.-Q.; Wei, Y.-C.; Kuo, K.-H.; Wang, C.-H.; Liu, S.-H.; Liao, L.-S.; Hung, W.-Y.; Fu, L.-W.; Chuang, W.-T.; Qin, M.; Lu, X.; You, C.; Chi, Y.; Chou, P.-T. Polyatomic molecules with emission quantum yields > 20% enable efficient organic light-emitting diodes in the NIR(II) window. *Nat. Photonics* **2022**, *16*, 843−850.
(30) Xie, Y.; Liu, W.; Deng, W.; Wu, H.; Wang, W.; Si, Y.; Zhan, X.; Gao, C.; Chen, X.-K.; Wu, H.; Peng, J.; Cao, Y. Bright short-

wavelength infrared organic light-emitting devices. *Nat. Photonics* **2022**, *16*, 752−761.
(31) Erker, C.; Basché, T. The Energy Gap Law at Work: Emission Yield and Rate Fluctuations of Single NIR Emitters. *J. Am. Chem. Soc.* **2022**, *144*, 14053−14056.
(32) Runge, E.; Gross, E. K. U. Density-Functional Theory for Time-Dependent Systems. *Phys. Rev. Lett.* **1984**, *52*, 997−1000.
(33) Becke, A. D. A new mixing of Hartree-Fock and local density-functional theories. *J. Chem. Phys.* **1993**, *98*, 1372−1377.
(34) Frisch, M. J.; Trucks, G. W.; Schlegel, H. B.; Scuseria, G. E.; Robb, M. A.; Cheeseman, J. R.; Scalmani, G.; Barone, V.; Petersson, G. A.; Nakatsuji, H.; Li, X.; Caricato, M.; Marenich, A. V.; Bloino, J.; anesko, B. G.; Gomperts, R.; Mennucci, B.; Hratchian, H. P.; Ortiz, J. V.; Izmaylov, A. F.; Sonnenberg, J. L.; Williams-Young, D.; Ding, F.; Lipparini, F.; Egidi, F.; Goings, J.; Peng, B.; Petrone, A.; Henderson, T.; Ranasinghe, D.; Zakrzewski, V. G.; Gao, J.; Rega, N.; Zheng, G.; Liang, W.; Hada, M.; Ehara, M.; Toyota, K.; Fukuda, R.; Hasegawa, J.; Ishida, M.; Nakajima, T.; Honda, Y.; Kitao, O.; Nakai, H.; Vreven, T.; Throssell, K.; Montgomery, J. A., Jr.; Peralta, J. E.; Ogliaro, F.; Bearpark, M. J.; Heyd, J. J.; Brothers, E. N.; Kudin, K. N.; Staroverov, V. N.; Keith, T. A.; Kobayashi, R.; Normand, J.; Raghavachari, K.; Rendell, A. P.; Burant, J. C.; Iyengar, S. S.; Tomasi, J.; Cossi, M.; Millam, J. M.; Klene, M.; Adamo, C.; Cammi, R.; Ochterski, J. W.; Martin, R. L.; Morokuma, K.; Farkas, O.; Foresman, J. B.; Fox, D. J. *Gaussian 16, Rev. B.01*; Gaussian, Inc.: Wallingford, CT, 2016.
(35) Boese, A. D.; Martin, J. M. Development of density functionals for thermochemical kinetics. *J. Chem. Phys.* **2004**, *121*, 3405−3416.
(36) Mennucci, B.; Tomasi, J.; Cammi, R.; Cheeseman, J. R.; Frisch, M. J.; Devlin, F. J.; Gabriel, S.; Stephens, P. J. Polarizable continuum model (PCM) calculations of solvent effects on optical rotations of chiral molecules. *J. Phys. Chem. A* **2002**, *106*, 6102−6113.
(37) Lu, T.; Chen, F. Multiwfn: a multifunctional wavefunction analyzer. *J. Comput. Chem.* **2012**, *33*, 580−592.
(38) Shuai, Z. Thermal Vibration Correlation Function Formalism for Molecular Excited State Decay Rates. *Chin. J. Chem.* **2020**, *38*, 1223−1232.

https://doi.org/10.1021/acs.jpclett.4c02023
J. Phys. Chem. Lett. 2024, 15, 9844−9851